

# Self-formed grain boundary healing layer for highly efficient $\text{CH}_3\text{NH}_3\text{PbI}_3$ perovskite solar cells

Dae-Yong Son<sup>1†</sup>, Jin-Wook Lee<sup>1†</sup>, Yung Ji Choi<sup>2</sup>, In-Hyuk Jang<sup>1</sup>, Seonhee Lee<sup>3</sup>, Pil J. Yoo<sup>4</sup>, Hyunjung Shin<sup>3\*</sup>, Namyoung Ahn<sup>5</sup>, Mansoo Choi<sup>5</sup>, Dongho Kim<sup>2\*</sup> and Nam-Gyu Park<sup>1\*</sup>

**Perovskite solar cells have attracted significant research efforts due to their remarkable performance, with certified power conversion efficiency now reaching 22%. Solution-processed perovskite thin films are polycrystalline, and grain boundaries are thought to be responsible for causing recombination and trapping of charge carriers. Here we report an effective and reproducible way of treating grain boundaries in  $\text{CH}_3\text{NH}_3\text{PbI}_3$  films deposited by means of a Lewis acid-base adduct approach. We show by high-resolution transmission electron microscopy lattice images that adding 6 mol% excess  $\text{CH}_3\text{NH}_3\text{I}$  to the precursor solution resulted in a  $\text{CH}_3\text{NH}_3\text{I}$  layer forming at the grain boundaries. This layer is responsible for suppressing non-radiative recombination and improving hole and electron extraction at the grain boundaries by forming highly ionic-conducting pathways. We report an average power conversion efficiency of 20.1% over 50 cells (best cell at 20.4%) together with significantly reduced current-voltage hysteresis achieved by this grain boundary healing process.**

Perovskite solar cells, receiving a great deal of attention due to low cost and high efficiency, are regarded as a promising photovoltaic technology. A surge of recent research activity in perovskite solar cells has been triggered by groundbreaking research on solid-state perovskite solar cells with a power conversion efficiency (PCE) of 9.7% (ref. 1) following two important seminal studies on redox-electrolyte-based perovskite-sensitized solar cells<sup>2,3</sup>. The development of a planar heterojunction structure<sup>4</sup> and a sequential deposition process<sup>5</sup> has pushed the PCE of perovskite solar cell towards 15%. Reports on unusual behaviours of amphoteric charge transport, long carrier diffusion, and charge accumulation in organolead halide perovskites<sup>6–10</sup> have provided insights into the superb photovoltaic performance of perovskite solar cells. As a result of a better understanding of the optoelectronic properties of perovskite, a certified PCE as high as 20.1% was achieved using mixed organic cations and halide anions<sup>11</sup>. Certified PCEs of up to 22% have since been reported<sup>12</sup>.

The primary materials for high efficiency perovskite solar cells reported thus far have been based on methylammonium lead iodide ( $\text{MAPbI}_3$ , where  $\text{MA} = \text{CH}_3\text{NH}_3$ ) and spiro-MeOTAD (2,2',7,7'-Tetrakis[N,N-di(4-methoxyphenyl)amino]-9,9'-spirobifluorene). A solution process has been widely adopted to form the  $\text{MAPbI}_3$  layer on suitable substrates, where grain size can be affected and a grain boundary is unavoidably formed<sup>13–15</sup>. Most studies have focused on high-quality perovskite films showing the longer photoluminescence (PL) decay property, because such films exhibited a better photovoltaic performance<sup>16</sup>.

The dependence of physico-chemical properties on grain boundaries has been extensively investigated for various materials. For instance, the thermoelectric property was substantially improved by dense dislocation arrays formed at grain boundaries in bismuth antimony telluride owing to the significant reduction in lattice thermal conductivity<sup>17</sup>. The importance of grain boundaries in electrical

conductance was emphasized for graphene because scattering of charge carriers at grain boundaries could degrade conductivity, and electrical conductance was found to be improved by interdomain connectivity in boundaries<sup>18</sup>. The optoelectronic properties of two-dimensional molybdenum disulfide were found to depend on the grain boundary structures—the optical property was improved at the tilt boundaries whereas in-plane electrical conductivity was better for the mirror twin boundaries<sup>19</sup>. Recently, the PL intensity and lifetime were reported to be different between grains in the same perovskite, where the grain boundaries exhibited less pronounced PL intensity along with a faster non-radiative decay<sup>20</sup>. This indicates that grain boundaries in organolead halide perovskite may play an important role in charge carrier kinetics, and thereby affect the photovoltaic performance. This also underlines that removal of any non-radiative pathways in grain boundaries may further improve the photovoltaic performance. The role of grain boundaries in affecting the photovoltaic properties of perovskite solar cell has been investigated. For example, the crucial role of grain boundaries in charge separation and collection was recently emphasized<sup>21</sup>. Also, it was demonstrated that a self-induced  $\text{PbI}_2$  layer at a grain boundary led to enhanced photovoltaic performance<sup>22</sup>. Therefore, effective management of grain boundaries is essential for high-performance perovskite solar cells.

Here, we report the production of highly efficient and reproducible  $\text{MAPbI}_3$  perovskite solar cells through a grain boundary healing process. A thin MAI layer was self-formed on  $\text{MAPbI}_3$  grains by spin coating of the precursor solution with a slight excess of MAI using a Lewis acid-base adduct approach<sup>23</sup>. The self-formed thin MAI layer was investigated by scanning transmission electron microscopy (STEM) with a high-angle annular dark-field detector. The carrier lifetime and exciton population were studied using transient absorption spectra. Charge extraction by linearly increasing voltage (CELIV) was carried out

<sup>1</sup>School of Chemical Engineering and Department of Energy Science, Sungkyunkwan University, Suwon 440-746, Korea. <sup>2</sup>Department of Chemistry, Yonsei University, Seoul 120-749, Korea. <sup>3</sup>Department of Energy Science, Sungkyunkwan University, Suwon 440-746, Korea. <sup>4</sup>School of Chemical Engineering and SKKU Advanced Institute of Nano Technology, Sungkyunkwan University, Suwon 440-746, Korea. <sup>5</sup>Department of Mechanical and Aerospace Engineering, Seoul National University, Seoul 151-744, Korea. <sup>†</sup>These authors contributed equally to this work. \*e-mail: hshin@skku.edu; dongho@yonsei.ac.kr; npark@skku.edu

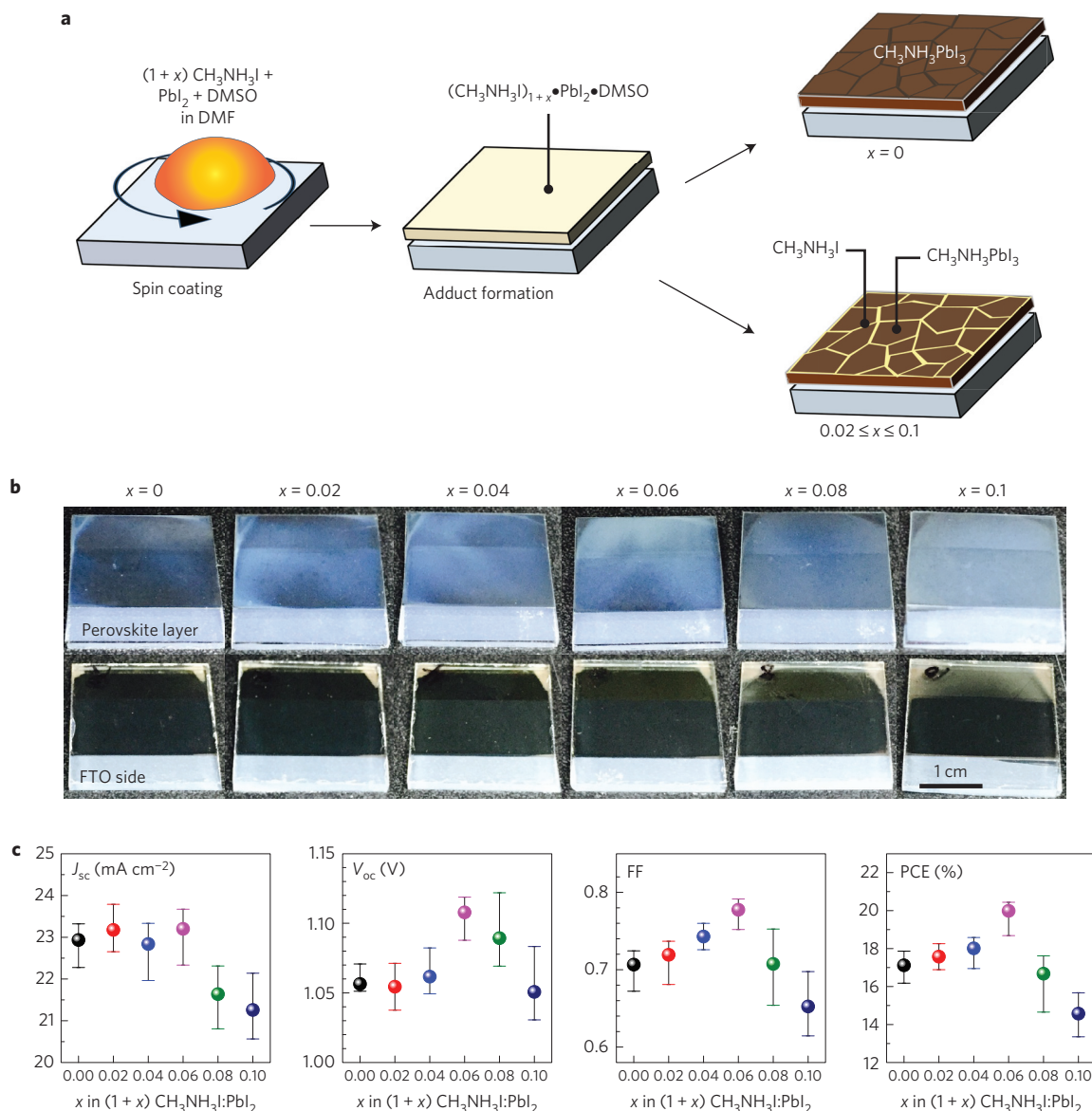


**Figure 1 | Effects of excess  $\text{CH}_3\text{NH}_3\text{I}$  on film and photovoltaic parameters. **a**, Schematic representation of the coating process used to form the  $\text{CH}_3\text{NH}_3\text{PbI}_3$  perovskite films with and without grain boundary healing layer via Lewis acid–base adduct intermediates. **b**, Photographs of the coated  $\text{CH}_3\text{NH}_3\text{PbI}_3$  films prepared from a non-stoichiometric precursor solution with excess  $\text{CH}_3\text{NH}_3\text{I}$ . Photographs were taken both from the perovskite layer and FTO sides. **c**, Plots of  $J_{\text{sc}}$ ,  $V_{\text{oc}}$ , FF and PCE as a function of  $x$  in  $(1+x) \text{CH}_3\text{NH}_3\text{I}:\text{PbI}_2$ . The data are average values determined from the reverse and forward scanned current–voltage curves. The high and low marks in **c** represent maximum and minimum values, respectively, and the filled circles are mean values.**

to investigate the change in charge mobility induced by the grain boundary healing process. Conducting atomic force microscopy (c-AFM) was carried out to investigate conduction on the grain boundaries through local current–voltage measurements. The grain boundary healing process was found to improve the photovoltaic performance, and was especially beneficial to the voltage and fill factor, eventually resulting in a best power conversion efficiency (PCE) of 20.4% and an average PCE of 20.1% from 50 cells.

### Self-formed grain boundary by excess MAI

The non-stoichiometric precursor solutions are prepared by mixing MAI,  $\text{PbI}_2$  and  $N,N'$ -dimethylsulfoxide (DMSO) in  $N,N'$ -dimethylformamide (DMF), where the molar ratio of  $\text{PbI}_2$ :MAI is changed from 1:1 to 1:1.02, 1:1.04, 1:1.06, 1:1.08 and 1:1.1 ( $x = 0, 0.02, 0.04, 0.06, 0.08$  and  $0.1$ ). The DMSO content is the same as  $\text{PbI}_2$ . The use of a non-stoichiometric precursor solution containing excess MAI was reported, in which

the excess MAI was used to compensate the loss of MAI during the grain-coarsening step at an elevated temperature of  $150^\circ\text{C}$  for 15 min. In this work, we use the precursor chemistry of the Lewis acid–base adduct method<sup>23</sup> to achieve highly efficient device performance. Since the stoichiometric 1:1:1 adduct of  $\text{PbI}_2$ , MAI and DMSO ( $\text{MAI} \cdot \text{PbI}_2 \cdot \text{DMSO}$ ) can be formed as an intermediate, excess MAI excluded from the adduct will not be formed in the  $\text{MAPbI}_3$  lattices, but possibly located at the grain boundary. The coating process is presented schematically in Fig. 1a, in which we expect that grain boundaries will form from the stoichiometric precursor coating solution ( $x = 0$ ) and that excess MAI will form on the  $\text{MAPbI}_3$  grains because it may not be taken up in the perovskite lattice. This seems to be a valid assumption because of the slightly turbid appearance of the films for  $0.02 < x < 0.1$  and the increasing turbidity with increasing MAI content (Fig. 1b). Thermogravimetric analysis confirms that MAI is not dissociated during the heat treatment at  $100^\circ\text{C}$  (Supplementary Fig. 1, 99.6

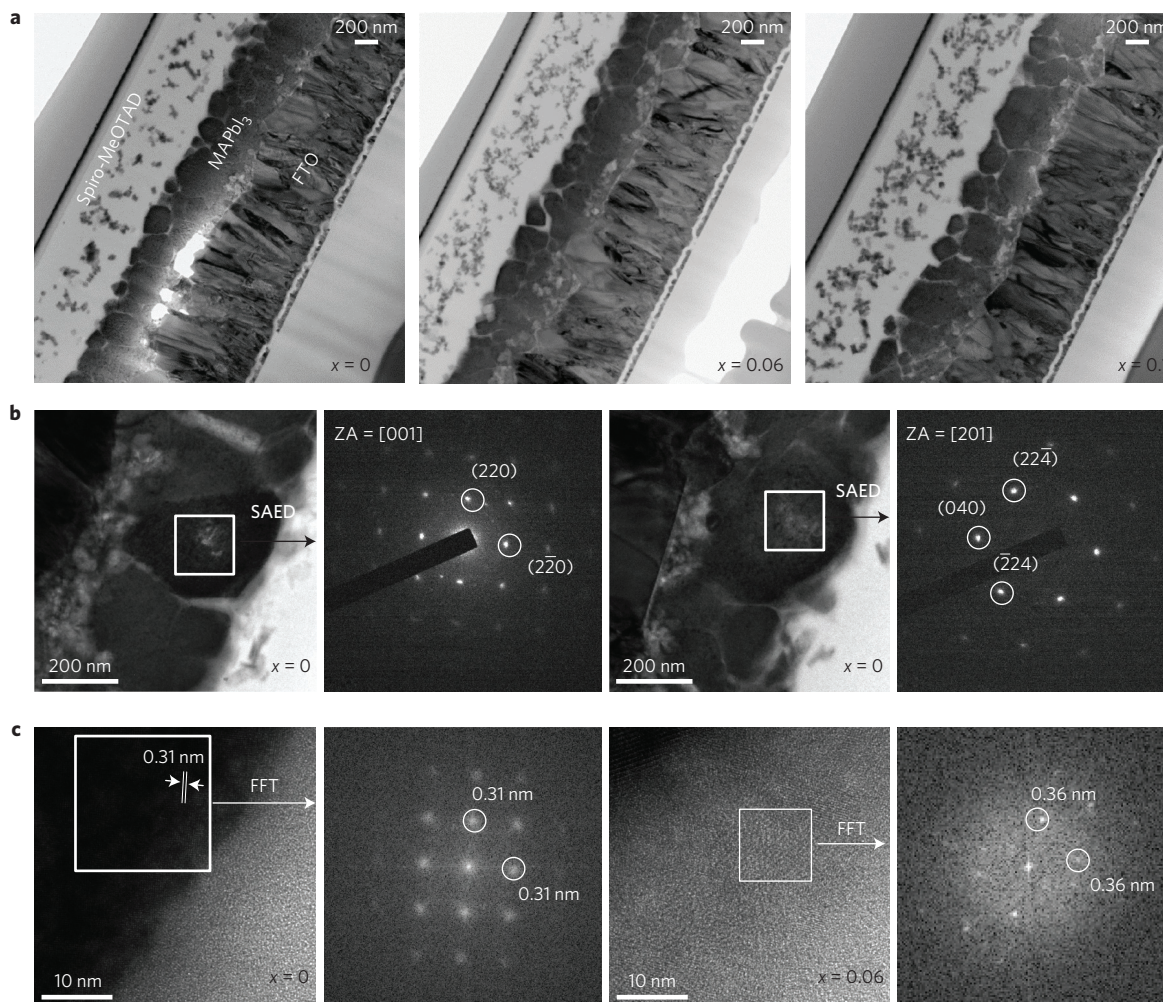


**Figure 2 | Grain and grain boundary analysis.** **a**, Cross-sectional TEM images of samples  $x = 0, 0.06$  and  $0.1$  with the glass/FTO/mp-TiO<sub>2</sub>/MAPbI<sub>3</sub>/spiro-MeOTAD configuration. **b**, Cross-sectional TEM bright-field images with the corresponding selected area electron diffraction (SAED) pattern for  $x = 0$ . **c**, High-resolution TEM lattice fringes for  $x = 0$  and  $0.06$  along with fast Fourier transformed (FFT) images.

wt% of the initial MAI remained at 212.2 °C). It is noted that the MAPbI<sub>3</sub> films look similar regardless of MAI content when viewing from the FTO (fluorine-doped tin oxide) side, which underlines that grain boundaries may be less pronounced in the perovskite film close to the FTO. Little difference in absorbance is observed regardless of the MAI content, but the reflectance is different, as can be seen in Supplementary Fig. 2, which indicates that unreacted MAI is likely to form on the surface of perovskite grains.

The photovoltaic parameters, listed in Supplementary Table 1, are found to be influenced by MAI content (Fig. 1c). The short-circuit photocurrent density ( $J_{sc}$ ) hardly changes up to  $x = 0.06$ , but declines slightly for  $x = 0.08$  and  $0.1$ . The average  $J_{sc}$  values determined by the reverse and forward scanned current–voltage curves are 23.89, 23.63, 23.72, 23.40, 22.87 and 22.76 mA cm<sup>-2</sup> for  $x = 0, 0.02, 0.04, 0.06, 0.08$  and  $0.1$ , respectively. On the other hand, both the open-circuit voltage ( $V_{oc}$ ) and fill factor (FF) are significantly altered. The average  $V_{oc}$  increases from 1.029 V for  $x = 0$  to 1.043, 1.050 and 1.118 V for  $x = 0.02, 0.04$  and  $0.06$ , respectively.  $V_{oc}$  is maximized at  $x = 0.06$ , then drops slightly to 1.079 and 1.061 V for higher MAI contents of  $x = 0.08$  and  $x = 0.1$ , respectively. The average FF shows a similar tendency. FF increases from 0.683 for  $x = 0$  to 0.727 and 0.726 for  $x = 0.02$  and  $0.04$ , respectively, reaching a maximum of 0.755 for  $x = 0.06$ , then decreases to 0.625 and 0.614 for higher MAI contents of  $x = 0.08$  and  $0.1$ , respectively. As a result, the average PCE increases from 16.8%

for the stoichiometric precursor solution to 19.8% for  $x = 0.06$ , while the high content of  $x = 0.1$  shows a lower PCE of 14.9%. The optimal concentration for the highest performance is thus determined to be  $x = 0.06$ . Higher contents of  $x > 0.06$  degrade rather than improve the photovoltaic performance.

An excess of MAI in the precursor coating solution hardly changes the tetragonal crystal structure and lattice constants, as can be seen in the X-ray diffraction (XRD) pattern in Supplementary Fig. 3, which indicates that the unreacted MAI is likely to exist on the perovskite grain surfaces. High-resolution STEM studies were carried out to investigate the probable existence of MAI on the grain boundaries. The whole device is cross-sectioned by means of a focused ion beam (FIB). In Fig. 2a, perovskite grains are clearly seen for the  $x = 0, 0.06$  and  $0.1$  samples. Selected area electron diffraction (SAED) studies on the perovskite grains result in distinct spot patterns corresponding to a single-crystalline structure (Fig. 2b). We observe two spot patterns corresponding to two zone axes of [001] and [201], which is consistent with the calculated electron diffraction pattern (Supplementary Fig. 4) and a tetragonal crystal system with space group of  $I4cm$  (ref. 24). The observed spot pattern for the zone axis of [001] agrees well with a previous report<sup>25</sup>. The lattice fringes are shown in Fig. 2c, where the inter-planar spacing of 0.31 nm for the  $x = 0$  sample is indexed to the (220) plane of crystalline CH<sub>3</sub>NH<sub>3</sub>PbI<sub>3</sub> grains. A fast Fourier transformed (FFT) image leading to the spot pattern<sup>24</sup> is in good agreement with the

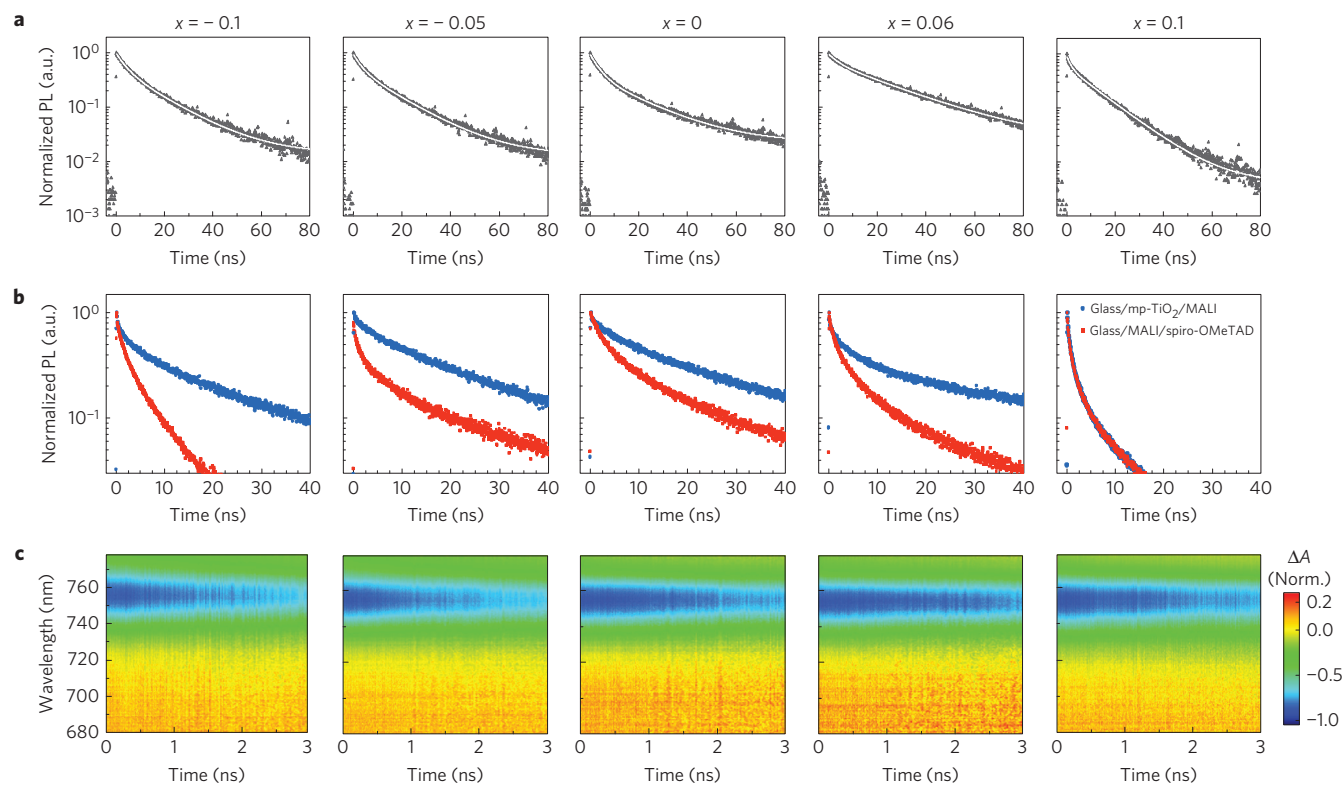


**Figure 3 | Photophysical characteristics for excess and deficient CH<sub>3</sub>NH<sub>3</sub>I.** **a, b**, Time-resolved PL spectra for the MAPbI<sub>3</sub> perovskite films without (**a**) and with (**b**) a carrier transporting layer of spiro-OMeTAD or mp-TiO<sub>2</sub>. Filled circles represent measured data while solid lines represent best fit results. The molar concentration of MAI precursor varies from 0.9 to 1.1 with respect to one mole of PbI<sub>2</sub> ( $x = -0.1, -0.05, 0, 0.06, 0.1$ , from left to right). For the photophysical measurements, perovskite films were prepared identically to the active layer of the practical perovskite solar cell devices. A pulsed (800 kHz) excitation at 400 nm with a fluence of 20 nJ cm<sup>-2</sup> per pulse impinging on the glass substrate side. **b**, Solid lines represent the decay profiles of  $\tau_{CT}$ , resulting from mp-TiO<sub>2</sub> (blue) or spiro-OMeTAD (red). **c**, Normalized two-dimensional TA spectra of the MAPbI<sub>3</sub> perovskite thin films without a carrier transporting layer. Each spectrum is normalized by setting its minimum value to -1. The samples were excited at 400 nm with a fluence of 0.8  $\mu\text{J cm}^{-2}$  per pulse.

observed SAED pattern for the zone axis of [001] in Fig. 2b. On the other hand, a new lattice fringe at 0.36 nm is observed on the surface of the CH<sub>3</sub>NH<sub>3</sub>PbI<sub>3</sub> grain for the  $x = 0.06$  sample. The FFT image shows a different electron diffraction pattern, which can be assigned to the (110) plane of MAI. The powder XRD pattern is obtained from the powdered MAI (Supplementary Fig. 5 and Supplementary Table 2), which is indexed as a tetragonal crystal system (JCPDF card no. 010-0737). The XRD peak at  $2\theta = 24.538^\circ$  arises from the (110) lattice plane and corresponds to a  $d$  spacing of 0.362 nm. Thus, the unreacted MAI for the  $x = 0.06$  samples is self-formed and crystallized on the perovskite grains with a tetragonal structure. We also find from plane-view SEM images in Supplementary Fig. 6 that the stepped edges of grains for  $x = 0$  disappear in the presence of excess MAI, which is also indicative of a modification of the surfaces of perovskite grains by excess MAI.

### Enhanced properties by self-formed grain boundary

Photophysical measurements on perovskite structures, with different MAI concentrations, were performed to find the reason for the outstanding and highly reproducible performance of the perovskite solar cell for  $x = 0.06$ . Time-resolved PL decay profiles and transient absorption (TA) spectra of perovskite films are shown in Fig. 3a–c, respectively, where a series of perovskite films were deposited directly on the glass substrate without (Fig. 3a,c) and with (Fig. 3b) an electron transporting layer (ETL) or a hole transporting layer (HTL) layer. Since it was reported that excess PbI<sub>2</sub> has a beneficial effect on the photovoltaic performance<sup>26,27</sup>, the surface composition (PbI<sub>2</sub> or MAI) of the grain boundary may affect

the charge carrier dynamics. Therefore, we prepared perovskite films with excess PbI<sub>2</sub>, such as MAI:PbI<sub>2</sub> = 0.9:1 ( $x = -0.1$ ) and 0.95:1 ( $x = -0.05$ ), for comparison with excess MAI cells. All the spectroscopic measurements were carried out at energy densities under 1  $\mu\text{J cm}^{-2}$  in which carrier annihilation and non-geminate recombination can be minimized<sup>28</sup>. The PL decays of a series of perovskite films on the glass substrate without E(H)TL, monitored at the peak emission ( $\sim 770$  nm), show bi-exponential decays (Fig. 3a) with fast ( $\tau_1 = 3.7 \pm 0.3$  ns for  $x = -0.1 \sim 0.06$  and  $\tau_1 = 1.7$  ns for  $x = 0.1$ ) and slow components ( $\tau_2 = 13\text{--}25$  ns); the detailed trace fit data are listed in Supplementary Table 3. We assign  $\tau_1$  as a decay component closely related to non-radiative recombination by defects (surface trap near grain boundaries) and  $\tau_2$  as a component of radiative recombination from bulk perovskite<sup>8,29,30</sup>. The sample with excess MAI ( $x = 0.06$ ) possesses the largest number of carriers remaining after 80 ns, which is attributed to strongly suppressed non-radiative recombination at grain boundaries ( $\tau_1$ ); also, in terms of Schottky disorder, the longest  $\tau_2$  component (24.9 ns) shown at  $x = 0.06$  may suggest an improved quality of bulk perovskite as a result of excess MAI. The shorter  $\tau_2$  at  $x = 0.1$ , however, implies that excess MAI above a critical concentration ( $x > 0.06$ ) degrades the quality of perovskite itself. The reduced non-radiative recombination for  $x = 0.6$  relative to  $x = 0$  is also confirmed by the enhanced steady-state PL intensity, as shown in Supplementary Fig. 7.

In Fig. 3b, a series of perovskite films with spiro-MeOTAD HTL or mp-TiO<sub>2</sub> ETL exhibit bi-exponential decay with a much faster decay component,  $\tau_{CT}$ , which is supposed to originate from

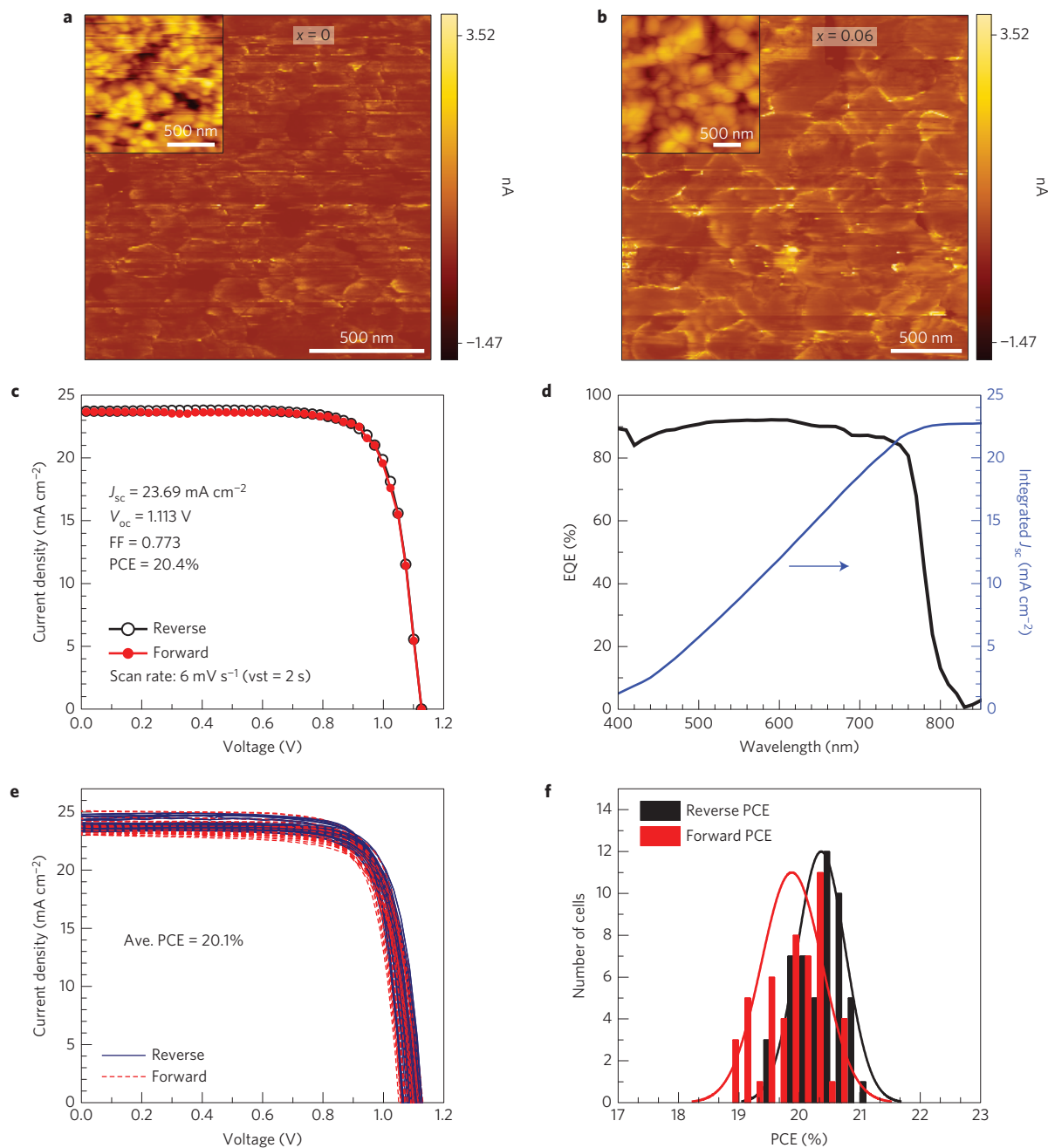


**Figure 4 | c-AFM and photovoltaic performance.** **a, b**, c-AFM images for the MAPbI<sub>3</sub> perovskite films for  $x = 0$  (**a**) and 0.06 (**b**) obtained at a bias voltage of 2 V in the dark, where the perovskite films were sandwiched by metal electrodes (FTO and Pt tip). Insets show the corresponding topographies. **c**,  $J$ - $V$  curves of the perovskite solar cell employing MAPbI<sub>3</sub> for  $x = 0.06$ , measured in reverse and forward scans at a scan rate of  $6 \text{ mV s}^{-1}$  (=voltage settling time of 2 s). **d**, EQE spectrum and the integrated  $J_{sc}$  based on the EQD data. **e**, Reverse and forward scanned  $J$ - $V$  curves for 50 cells obtained at a scan rate of  $6 \text{ mV s}^{-1}$  (=voltage settling time of 2 s). **f**, Histogram of the PCEs for the reverse and forward scanned data for 50 cells. Solid lines represent statistical data binning results.

carrier extraction by the layers<sup>6,7,31</sup>, the long component ( $\tau_{\text{unq}}$ ) implies the existence of unquenched carriers in thick perovskite films<sup>32</sup>. Decay profiles were fitted with values of  $\tau_{CT}$ s, which are known as  $\sim 0.64$  and  $\sim 1$  ns for spiro-MeOTAD and a 50-nm-thick mp-TiO<sub>2</sub> layer, respectively<sup>7,31</sup> (see Supplementary Table 3). It is noteworthy that the non-stoichiometric samples ( $x \neq 0$ ), including sample with either excess MAI or PbI<sub>2</sub>, exhibit a large amplitude for the  $\tau_{CT}$  component ( $A_{CT} > 40\%$ ), indicative of more efficient carrier extraction than stoichiometric samples ( $x = 0$ ), which supports our photovoltaic characteristics and recent study<sup>26</sup>. Although efficient carrier extraction occurs even in  $x = 0.1$  samples,

$\tau_2$  ( $\sim \tau_{\text{unq}}$ ) decreases at the same time; therefore, this faster carrier recombination (which includes radiative and non-radiative hole-electron recombination) is supposed to be the reason for lower performances with  $x = 0.1$ .

We tried to investigate the defect-mediated recombination dynamics ( $\tau_1$ ) of perovskite films by measuring their TA spectra from the picosecond to the nanosecond regime. The normalized TA two-dimensional colour maps of the bare perovskite samples are presented in Fig. 3c. All the samples were excited at 400 nm ( $0.8 \mu\text{J cm}^{-2}$ ). It has been previously reported that pump-induced carriers occupy the conduction band, which gives rise to the

photo-induced bleaches (blue signal); moreover, the features at 775 nm can be assigned to stimulated emission by comparison with the steady-state PL spectrum (Supplementary Fig. 8)<sup>33,34</sup>. As shown in Fig. 3c, the invariance of the peak position (wavelength) with varying concentration suggests that the non-stoichiometry of precursor solution has little effect on the band gap. On the other hand, the decay of the bleach signal shows a strong dependence on the composition; it lasts longer on increasing from  $x = -0.1$  to  $x = 0.06$  (longest), which is consistent with the time-resolved PL results in Fig. 3a. These photophysical results clearly show that the MAI formed on the grain boundaries has a protective effect on charge carriers, which can easily recombine at or near grain boundaries. In particular, hole and electron extraction are higher at  $x = 0.06$ , which may be attributed to localized states induced by excess MAI above and below the valence and conduction bands<sup>35</sup>. As a result, we conclude that the outstanding performance of perovskite layers prepared with excess MAI, especially for  $x = 0.06$ , is associated with suppressed carrier recombination at and near grain boundaries, maximized charge extraction on perovskite/H(E)TL interfaces, and possibly improvements in the quality of the perovskite layer. The effect of non-passivated grain boundaries on the performance of perovskite solar cells has been reported: the structural disorder at/near grain boundaries, such as vacancy or interstitial defects, forms detrimental charge trap states<sup>36–40</sup>. The trap states can act as a charge recombination centre, resulting in a lower quasi Fermi level and reduced carrier mobility, which consequently reduces  $V_{oc}$  and FF. Recent reports<sup>40–44</sup> have demonstrated that passivating the grain boundaries, using such agents as  $Cl^-$ , PCBM (phenyl-C61-butyric acid methyl ester), pyridine and  $PbI_2$ , can mitigate the effect of the trap states mentioned above. In our study, using photophysical and electrical measurements, we demonstrated that samples with MAI excess show a lower amount of initial decay (trap-mediated recombination) and enhanced  $V_{oc}$  and FF, which implies that remnant MAI at the grain boundary can effectively passivate the structural defects at/near the grain boundaries.

Charge extraction by linearly increasing voltage (CELIV) was carried out under illumination to investigate any change in charge mobility due to the self-formed MAI layer (Supplementary Fig. 9). The perovskite layer including a mesoporous  $TiO_2$  layer was fixed to a thickness of approximately 600 nm. The charge mobility for  $x = 0$  is estimated to be  $1.2 \times 10^{-3} \text{ cm}^2 \text{ Vs}^{-1}$ , which is in good agreement with previous results<sup>23,45</sup>. The charge mobility increases by one order of magnitude ( $1.08 \times 10^{-2} \text{ cm}^2 \text{ Vs}^{-1}$ ) for  $x = 0.06$ . A mobility of  $9.66 \times 10^{-3} \text{ cm}^2 \text{ Vs}^{-1}$  is observed for  $x = 0.1$ , which is higher than that of the pristine  $x = 0$  sample, but slightly lower than that for  $x = 0.06$ . The significant increase in charge mobility for the excess MAI is consistent with the PL and TA data.

### Improved conductance and efficiency over 20%

Figure 4a,b shows c-AFM images under a bias voltage of 2 V, along with the corresponding topological images in the insets. Brighter contrast in Fig. 4a,b indicates more conducting current flow through the perovskite layer<sup>46</sup>. In general a greater current through the perovskite ( $x = 0.06$ ) sample than the  $x = 0$  sample has been observed. Moreover, in Fig. 4b, grain boundaries showing brighter contrast indicate that the grain boundary carries the current more efficiently. Superimposing the line profiles of topography and current images spatially confirms more current through the grain boundaries, as shown in Supplementary Fig. 10. The grain boundaries, MAIs, can clearly be considered as charge transporting channels. Although the nature of charge transport is unclear, it is most likely ionic<sup>47</sup>. Clear rectifying behaviour is also observed in the sample ( $x = 0.06$ ) from the local current–voltage measurement, as shown in Supplementary Fig. 11. From a statistical point of view, much more reliable rectifying behaviour is obtained in the  $x = 0.06$  sample than the  $x = 0$  sample. Higher  $V_{oc}$  for the sample

with  $x = 0.06$  implies reduced charge recombination with MAI layers at the grain boundary. The self-formed grain boundaries are likely to contribute to the enhanced photovoltaic performances by facilitating not only charge separation, but also charge transport, rather than acting as recombination centres, as is the case in conventional grain boundaries.

Based on the  $x = 0.06$  sample, the best PCE of 20.4% is obtained from averaging the reverse scanned data of  $J_{sc} = 23.72 \text{ mA cm}^{-2}$ ,  $V_{oc} = 1.117 \text{ V}$ , FF = 0.779 and PCE = 20.6% and the forward scanned data of  $J_{sc} = 23.67 \text{ mA cm}^{-2}$ ,  $V_{oc} = 1.110 \text{ V}$ , FF = 0.768 and PCE of 20.2% (Fig. 4c). The external quantum efficiency (EQE) demonstrates the high quantum yield throughout the entire wavelength range (Fig. 4d), leading to an accumulated photocurrent density of  $22.77 \text{ mA cm}^{-2}$ , which is close to the  $J_{sc}$  measured under white light (one sun). We obtained a mean PCE of 20.1% from 50 cells (Supplementary Table 4), based on the averaged values of the reverse and forward scanned  $I-V$  data (Fig. 4e,f). The steady-state  $J_{sc}$  and PCE measured at the maximum voltage, as obtained from the power curve, are stable for the  $x = 0$  and  $x = 0.06$  cases, but degrade for  $x = 0.1$  (Supplementary Fig. 12), which indicates that the stability is dependent on the self-formed MAI concentration and that an MAI content less than 0.06 can guarantee stability. Regarding current–voltage hysteresis, the self-formed MAI layer ( $x = 0.06$ ) reduces the hysteresis relative to the equimolar case ( $x = 0$ ), as can be seen Supplementary Table 1. In addition, although the hysteresis is affected by the selective contacts<sup>48</sup>, we find that the environmental conditions for fabricating perovskite films even with the same selective contacts have a significant effect on the hysteresis. The perovskite films with  $x = 0.06$  prepared at temperature lower than  $20^\circ \text{C}$  and relative humidity less than 25% show negligible hysteresis (Supplementary Fig. 13) at a scan rate of  $6 \text{ mV s}^{-1}$ , which suggests that careful control of both temperature and humidity is required for the grain boundary healing process to reduce the hysteresis. Since the hysteresis is greatly suppressed by the grain boundary healing layer comprising MAI, excess  $PbI_2$  may be expected to show a similar effect. However, severe hysteresis is observed for the deficient MAI samples with  $x = -0.1$  and  $-0.05$ , as can be seen in Supplementary Fig. 14, due to instability of the photocurrent with time (Supplementary Fig. 15).

### Conclusion

In conclusion, an effective passivation layer was reproducibly introduced on  $MAPbI_3$  perovskite grain boundaries by one-step spin coating of a precursor solution containing excess MAI in equimolar  $PbI_2$  and DMSO by means of a Lewis acid–base adduct approach. This grain boundary healing process was found to play a crucial role in carrier lifetime improvement, suppression of non-radiative recombination at grain boundaries, and effective extraction of charge carriers at the interface between perovskite and selective contacts. A continuous and pronounced conducting pathway through grain boundaries was produced by the self-formed grain boundary of MAI. Consequently, the photovoltaic performance was improved by the self-formed MAI layer on the grain boundaries of  $MAPbI_3$ , leading consistently to average power conversion efficiencies exceeding 20%. In addition, an optimal concentration of MAI, such as  $x = 0.06$  in a  $(1+x)$  MAI +  $PbI_2$  mixture, resulted in a significant reduction in  $I-V$  hysteresis along with a stable photocurrent. The efficiency that we obtained is the highest value so far for the pure  $CH_3NH_3PbI_3$  perovskite (reported efficiencies in excess of 21% were based on mixed cations and anions).

### Methods

**Synthesis of  $CH_3NH_3I$ .** Methylammonium iodide MAI ( $MA = CH_3NH_3$ ) was synthesized as reported elsewhere<sup>13,13</sup>. 30 ml of hydroiodic acid (57 wt% in water, Aldrich) was reacted with 27.8 ml of methylamine (40 wt% in methanol, TCI) at  $0^\circ \text{C}$  for 2 h. From the solution, a dark brown precipitate was recovered using

a rotary evaporator at 60 °C for 2 h. The resulting precipitate was washed with diethyl ether several times until the colour of the precipitate changed to white, and then recrystallized from ethanol. The white precipitate was collected by filtration and dried under vacuum for 24 h before storage in a glove box filled with Ar.

**Device fabrication.** The FTO glass (Pilkington, TEC-8,  $8 \Omega \text{sq}^{-1}$ ) was cleaned with detergent and ethanol, then further treated with ultraviolet–ozone for 20 min to remove organic contaminants. To form the compact  $\text{TiO}_2$  blocking layer (bl- $\text{TiO}_2$ ), 0.15 M titanium diisopropoxide di(acetylacetonate) (Sigma-Aldrich, 75 wt% in isopropanol) in 1-butanol (Sigma-Aldrich, 99.8%) solution was spin-coated on the cleaned FTO glass at 251.55g for 20 s using a spin coater (WS 650 Spin Coater) and dried at 125 °C for 5 min. A mesoporous  $\text{TiO}_2$  (mp- $\text{TiO}_2$ ) layer was deposited on top of the bl- $\text{TiO}_2$  layer by spin-coating a diluted  $\text{TiO}_2$  paste (50-nm-sized  $\text{TiO}_2$  nanoparticles, terpineol, ethylcellulose and lauric acid with a nominal composition of 1.25:6:0.9:0.1 in wt%) in anhydrous 1-butanol ( $1 \text{ g ml}^{-1}$ ) at 111.8g for 20 s using a spin coater (WS 650 Spin Coater). The film was annealed at 550 °C for 1 h. After cooling down to room temperature, the film was exposed to ultraviolet–ozone for 20 min before being treated with 20 mM aqueous  $\text{TiCl}_4$  (Sigma-Aldrich,  $\geq 98\%$ ) solution at 90 °C for 10 min. The  $\text{TiCl}_4$ -treated film was cleaned with deionized water and annealed again at 500 °C for 30 min. To prepare the  $\text{MAI}_{1-x} \cdot \text{PbI}_2 \cdot \text{DMSO}$  adduct, 461 mg of  $\text{PbI}_2$ , MAI in amounts of 159.0 mg for  $x = 0$ , 162.2 mg for  $x = 0.02$ , 165.3 mg for  $x = 0.04$ , 168.5 mg for  $x = 0.06$ , 171.7 mg for  $x = 0.08$  and 174.9 mg for  $x = 0.1$ , and 78 mg of DMSO ( $>99.5\%$ , Sigma) were mixed in 494.3 mg of DMF (anhydrous, 99.8% Sigma-Aldrich), which was stirred at room temperature for 1 h before use. The precursor solution was spin-coated on the mp- $\text{TiO}_2$  at 698.75g for 25 s, into which 0.5 ml of diethyl ether was dropped after 10 s while spinning. The resulting yellowish transparent adduct films were converted to perovskite film by heating at 65 °C for 1 min and then at 100 °C for 2 min. The 20  $\mu\text{l}$  of spiro-MeOTAD solution, consisting of 72.3 mg spiro-MeOTAD (Merck), 28.8  $\mu\text{l}$  of 4-*tert*-butyl pyridine and 17.5  $\mu\text{l}$  of lithium bis(trifluoromethanesulfonyl)imide (Li-TFSI) solution (520 mg Li-TFSI in 1 ml acetonitrile (Sigma-Aldrich, 99.8%)) in 1 ml of chlorobenzene, was spin-coated on the perovskite layer at 251.55g for 30 s (refs 5,13). Finally, a Ag electrode approximately 120 nm in thickness was deposited by thermal evaporation at a constant evaporation rate of  $0.3 \text{ \AA s}^{-1}$ .

**Photocurrent density–voltage ( $J$ – $V$ ) measurements.** Photocurrent density–voltage ( $J$ – $V$ ) characteristics were measured under AM 1.5G one sun ( $100 \text{ mW cm}^{-2}$ ) illumination from a 450 W xenon lamp (Newport 6279NS), which was simulated by a solar simulator (Oriel Sol 3A, class AAA). The light intensity was adjusted by means of an NREL-calibrated Si solar cell equipped with a KG-2 filter. The device was covered with a metal mask with an aperture area of  $0.125 \text{ cm}^2$ . External quantum efficiency (EQE) was measured using an EQE system (PV measurement). The monochromatic beam was generated from a 75 W xenon lamp (USHIO). EQE data were collected in the DC mode<sup>49</sup>.

**Powder X-ray diffraction.** Powder X-ray diffraction patterns were obtained using a PW 1050 diffractometer (Philips) under graphite-monochromated Cu- $K\alpha$  radiation ( $\lambda = 1.54184 \text{ \AA}$ ). Surface and cross-sectional morphologies were investigated by means of a scanning electron microscope (SEM, JSM-7600F, JEOL). Absorption and reflectance spectra were measured using an ultraviolet/visible spectrometer (Lambda 45, Perkin Elmer).

**Charge extraction by linearly increasing voltage (CELIV).** Photo-CELIV was measured for the devices with the FTO/bl- $\text{Al}_2\text{O}_3$ /mp- $\text{TiO}_2$ /MAPbI<sub>3</sub>/spiro-MeOTAD/Ag configuration in ambient air conditions to investigate charge carrier mobility and charge extraction. The device structure was designed to collect holes by introducing an electron-non-injecting  $\text{Al}_2\text{O}_3$  layer (bl- $\text{Al}_2\text{O}_3$ ). A Nd:YAG laser (MINILITE I, Continuum; 532 nm, 12 mJ/pulse, pulse width 3–5 ns) illuminated the FTO side. After a delay of 2.85  $\mu\text{s}$  generated by a delay generator (DG535, Stanford Research Systems), a linearly increasing triangular voltage pulse generated by a function generator (DS345, Stanford Research Systems) was applied to the sample in reverse bias (positive and negative probe connected to the FTO and the Ag electrode, relatively). To suppress charge extraction by the built-in electric field, the applied offset voltage was  $-2.4 \text{ V}$  and the maximum applied voltage was  $2.4 \text{ V}$  for 50  $\mu\text{s}$ . Current transients were monitored through a  $50 \Omega$  load resistor to convert voltage to current using a digital oscilloscope (TDS3054B, Tektronix)<sup>50–53</sup>. Charge carrier mobility ( $\mu$ ) was calculated according to equation (1)<sup>54</sup>,

$$\mu = \frac{2d^2}{3At_{\text{max}}^2[1 + 0.36\frac{\Delta j}{j_0}]} \quad \text{if } \Delta j \leq j_0 \quad (1)$$

where  $d$  is the film thickness,  $A$  the voltage increase rate,  $t_{\text{max}}$  the time at maximum  $\Delta j$  of the extraction peak, and  $j_0$  the capacitive displacement current. To compare the charge extraction, the extraction peak  $\Delta j$  was normalized by  $j_0$  (ref. 13).

**Transmission electron microscopy.** The cross-sectional morphologies and structures of the full cells were investigated using a high-resolution transmission electron microscope. The samples were prepared by vertical etching using focused ion beam (FIB) equipment (SMI3050TB). The cross-sectional surface was *in situ* coated with platinum using the gas injection system (Zeiss CrossBeam) to protect the surface from damage during FIB milling. An FTO/ $\text{TiO}_2$ /perovskite/spiro-MeOTAD specimen approximately 60 nm in thickness was obtained. TEM images and SAED patterns were obtained using a high-resolution transmission electron microscope (JEOL JEM-2100F) at an acceleration voltage of 200 kV in the high-angle annular dark-field imaging mode.

**Time-resolved photoluminescence (PL) decay measurement.** Time-resolved photoluminescence was detected using a time-correlated single-photon counting (TCSPC) technique to measure the spontaneous photoluminescence decay. The excitation light source was a mode-locked Ti:sapphire laser (MaiTai BB, Spectra-Physics), which provides ultrashort pulses (80 fs full-width at half-maximum) with a high repetition rate (80 MHz). This high repetition rate may be slowed to 1 MHz–800 kHz using an in-house-built pulse picker. The pulse-picked output pulse was frequency-doubled (400 nm) by a 1-mm-thick BBO crystal (EKSMa). The photoluminescence was collected by a microchannel plate photomultiplier (R3809U-51, Hamamatsu) with a thermoelectric cooler (C4878, Hamamatsu) connected to a TCSPC board (SPC-130, Becker Hickl GmbH). The overall instrumental response function was  $\sim 30 \text{ ps}$  (full-width at half-maximum). A pump pulse, vertically polarized by a Glan-laser polarizer, was used to irradiate the samples, and a sheet polarizer, set at an angle complementary to the magic angle ( $54.7^\circ$ ), was placed in the photoluminescence collection path to obtain polarization-independent photoluminescence decays.

**Femtosecond transient absorption (fs-TA).** Femtosecond transient absorption was detected using a pump–probe method to measure differential absorption ( $\Delta A$ ) spectra and their decay profile. The excitation light source was a Ti:sapphire regenerative amplifier system (Integra-C) operating at a 1 kHz repetition rate. A small portion of the fundamental pulses (800 nm) was picked off by a quartz plate to produce a white light continuum (WLC). The WLC probe pulses were generated using a sapphire window (3 mm in thickness) by focusing fundamental pulses. The remaining pulses were frequency-doubled using a 1-mm-thick BBO crystal (EKSMa) to produce a 400-nm pump pulse. The pump pulses generated had a pulse width of  $\sim 100 \text{ fs}$  and an average power of 100 mW. Pump power was carefully controlled by a neutral density filter ( $0.8 \mu\text{J cm}^{-2}$  per pulse in front of perovskite film surface) to minimize the effect of carrier annihilation or non-geminate recombination. The time delay between pump and probe beam was carefully controlled in such a way that the pump beam travels along a variable optical delay (ILS250). The intensities of the spectrally dispersed WLC probe pulses were monitored by a high-speed spectrometer (Ultrafast Systems). To obtain the time-resolved transient absorption difference signal ( $\Delta A$ ) at a specific time, the pump pulses were modulated at 500 Hz by an optical chopper, and thereby absorption spectra intensities were saved alternately with or without a pump pulse. Typically, 10,000 spectra were averaged to obtain the fs-TA spectra at a particular delay time. The polarization angle between pump and probe beam was set at the magic angle ( $54.7^\circ$ ) using a Glan-laser polarizer with a half-wave retarder to prevent polarization-dependent signals. Cross-correlation (full-width at half-maximum) in the pump–probe experiments was less than 200 fs and the chirp of the WLC probe pulses was measured to be 800 fs in the 400–800-nm region. All samples were mounted in a liquid-nitrogen cryostat (OptistatDN2, Oxford Instruments), where they remained under vacuum ( $P < 10^{-2} \text{ mbar}$ ) during all the optical TA studies. After the fs-TA experiments, we carefully examined the absorption spectra of all sample series to see if there were any artefacts due to degradation and photo-oxidation of samples.

**Conductive atomic force microscopy (c-AFM).** A commercial atomic force microscope (SPA-400, SII) was employed, equipped with Pt/Ir-coated Si tips (CONTPT-W, Nanoworld) with a typical resonance frequency of 13 kHz and a spring constant of  $0.2 \text{ N m}^{-1}$ . All images were acquired with bias voltages of 0–5 V at scan rates of 0.5 Hz. Positive biases were applied to the substrate, while the tips were grounded. The current and topographic images were taken simultaneously in ambient conditions.

Received 11 January 2016; accepted 13 May 2016;  
published 20 June 2016

## References

- Kim, H.-S. *et al.* Lead iodide perovskite sensitized all-solid-state submicron thin film mesoscopic solar cell with efficiency exceeding 9%. *Sci. Rep.* **2**, 591 (2012).
- Kojima, A., Teshima, K., Shirai, Y. & Miyasaka, T. Organometal halide perovskites as visible-light sensitizers for photovoltaic cells. *J. Am. Chem. Soc.* **131**, 6050–6051 (2009).

3. Im, J.-H., Lee, C.-R., Lee, J.-W., Park, S.-W. & Park, N.-G. 6.5% efficient perovskite quantum-dot-sensitized solar cell. *Nanoscale* **3**, 4088–4093 (2011).
4. Liu, M., Johnston, M. B. & Snaith, H. J. Efficient planar heterojunction perovskite solar cells by vapour deposition. *Nature* **501**, 395–398 (2013).
5. Burschka, J. *et al.* Sequential deposition as a route to high-performance perovskite-sensitized solar cells. *Nature* **499**, 316–319 (2013).
6. Stranks, S. D. *et al.* Electron-hole diffusion lengths exceeding 1 micrometer in an organometal trihalide perovskite absorber. *Science* **342**, 341–344 (2013).
7. Xing, G. *et al.* Long-range balanced electron and hole-transport lengths in organic-inorganic  $\text{CH}_3\text{NH}_3\text{PbI}_3$ . *Science* **342**, 344–347 (2013).
8. Shi, D. *et al.* Low trap-state density and long carrier diffusion in organolead trihalide perovskite single crystals. *Science* **347**, 519–522 (2015).
9. Dong, Q. *et al.* Electron-hole diffusion lengths > 175 nm in solution-grown  $\text{CH}_3\text{NH}_3\text{PbI}_3$  single crystals. *Science* **347**, 967–970 (2015).
10. Kim, H.-S. *et al.* Mechanism of carrier accumulation in perovskite thin-absorber solar cells. *Nature Commun.* **4**, 2242 (2013).
11. Yang, W. S. High-performance photovoltaic perovskite layers fabricated through intramolecular exchange. *Science* **348**, 1234–1237 (2015).
12. *Best Research-Cell Efficiencies* (National Renewable Energy Laboratory, 2016); [http://www.nrel.gov/ncpv/images/efficiency\\_chart.jpg](http://www.nrel.gov/ncpv/images/efficiency_chart.jpg)
13. Im, J.-H., Jang, I.-H., Pellet, N., Grätzel, M. & Park, N.-G. Growth of  $\text{CH}_3\text{NH}_3\text{PbI}_3$  cuboids with controlled size for high-efficiency perovskite solar cells. *Nature Nanotech.* **9**, 927–932 (2014).
14. Li, W., Fan, J., Li, J., Mai, Y. & Wang, L. Controllable grain morphology of perovskite absorber film by molecular self-assembly toward efficient solar cell exceeding 17%. *J. Am. Chem. Soc.* **137**, 10399–10405 (2015).
15. Xiao, M. *et al.* A fast deposition-crystallization procedure for highly efficient lead iodide perovskite thin-film solar cells. *Angew. Chem.* **126**, 10056–10061 (2014).
16. Zhou, H. *et al.* Interface engineering of highly efficient perovskite solar cells. *Science* **345**, 542–546 (2014).
17. Kim, S. I. *et al.* Dense dislocation arrays embedded in grain boundaries for high-performance bulk thermoelectrics. *Science* **348**, 109–114 (2015).
18. Tsen, A. W. *et al.* Tailoring electrical transport across grain boundaries in polycrystalline graphene. *Science* **336**, 1143–1146 (2012).
19. van der Zande, A. M. *et al.* Grains and grain boundaries in highly crystalline monolayer molybdenum disulphide. *Nature Mater.* **12**, 554–561 (2013).
20. de Quilletes, D. W. *et al.* Impact of microstructure on local carrier lifetime in perovskite solar cells. *Science* **348**, 683–686 (2015).
21. Yun, J. S. *et al.* Benefit of grain boundaries in organic-inorganic halide planar perovskite solar cells. *J. Phys. Chem. Lett.* **6**, 875–880 (2015).
22. Chen, Q. *et al.* Controllable self-induced passivation of hybrid lead iodide perovskites toward high performance solar cells. *Nano Lett.* **14**, 4158–4163 (2014).
23. Ahn, N. *et al.* Highly reproducible perovskite solar cells with average efficiency of 18.3% and best efficiency of 19.7% fabricated via Lewis base adduct of lead(II) iodide. *J. Am. Chem. Soc.* **137**, 8696–8699 (2015).
24. Dang, Y. *et al.* Bulk crystal growth of hybrid perovskite material  $\text{CH}_3\text{NH}_3\text{PbI}_3$ . *CrystEngComm* **17**, 665–670 (2015).
25. Yang, M. *et al.* Square-centimeter solution-processed planar  $\text{CH}_3\text{NH}_3\text{PbI}_3$  perovskite solar cells with efficiency exceeding 15%. *Adv. Mater.* **27**, 6363–6370 (2015).
26. Roldán-Carmona, C. *et al.* High efficiency methylammonium lead triiodide perovskite solar cells: the relevance of non-stoichiometric precursors. *Energy Environ. Sci.* **8**, 3550–3556 (2015).
27. Kim, Y. C. *et al.* Beneficial effects of  $\text{PbI}_2$  incorporated in organo-lead halide perovskite solar cells. *Adv. Energy Mater.* **6**, 1502104 (2016).
28. Manser, J. S. & Kamat, P. V. Band filling with free charge carriers in organometal halide perovskites. *Nature Photon.* **8**, 737–743 (2014).
29. Yang, Y. *et al.* Low surface recombination velocity in solution-grown  $\text{CH}_3\text{NH}_3\text{PbBr}_3$  perovskite single crystal. *Nature Commun.* **6**, 7961 (2015).
30. Yan, W. *et al.* Stable high-performance hybrid perovskite solar cells with ultrathin polythiophene as hole-transporting layer. *Nano Res.* **8**, 2474–2480 (2015).
31. Yang, Y. *et al.* The size effect of  $\text{TiO}_2$  nanoparticles on a printable mesoscopic perovskite solar cell. *J. Mater. Chem. A* **3**, 9103–9107 (2015).
32. Wen, X. *et al.* Morphology and carrier extraction study of organic-inorganic metal halide perovskite by one- and two-photon fluorescence microscopy. *J. Phys. Chem. Lett.* **5**, 3849–3853 (2014).
33. Yang, Y. *et al.* Observation of a hot-phonon bottleneck in lead-iodide perovskites. *Nature Photon.* **10**, 53–59 (2016).
34. Wang, L. *et al.* Femtosecond time-resolved transient absorption spectroscopy of  $\text{CH}_3\text{NH}_3\text{PbI}_3$  perovskite films: evidence for passivation effect of  $\text{PbI}_2$ . *J. Am. Chem. Soc.* **136**, 12205–12208 (2014).
35. Sadhanala, A. *et al.* Preparation of single-phase films of  $\text{CH}_3\text{NH}_3\text{Pb}(\text{I}_{1-x}\text{Br}_x)_3$  with sharp optical band edges. *J. Phys. Chem. Lett.* **5**, 2501–2505 (2014).
36. Yu, H., Lu, H., Xie, F., Zhou, S. & Zhao, N. Native defect-induced hysteresis behavior in organolead iodide perovskite solar cells. *Adv. Funct. Mater.* **26**, 1411–1419 (2016).
37. Agiorgousis, M. L., Sun, Y. Y., Zeng, H. & Zhang, S. Strong covalency-induced recombination centers in perovskite solar cell material  $\text{CH}_3\text{NH}_3\text{PbI}_3$ . *J. Am. Chem. Soc.* **136**, 14570–14575 (2014).
38. Buin, A. *et al.* Materials processing routes to trap-free halide perovskites. *Nano Lett.* **14**, 6281–6286 (2014).
39. Yin, W.-J., Shi, T. & Yan, Y. Unusual defect physics in  $\text{CH}_3\text{NH}_3\text{PbI}_3$  perovskite solar cell absorber. *Appl. Phys. Lett.* **104**, 063903 (2014).
40. Yin, W.-J., Chen, H., Shi, T., Wei, S.-H. & Yan, Y. Origin of high electronic quality in structurally disordered  $\text{CH}_3\text{NH}_3\text{PbI}_3$  and the passivation effect of Cl and O at grain boundaries. *Adv. Electron. Mater.* **1**, 1500044 (2015).
41. Xu, J. *et al.* Perovskite–fullerene hybrid materials suppress hysteresis in planar diodes. *Nature Commun.* **6**, 7081 (2015).
42. de Quilletes *et al.* Impact of microstructure on local carrier lifetime in perovskite solar cells. *Science* **348**, 683–686 (2015).
43. Shao, Y., Xiao, Z., Bi, C., Yuan, Y. & Huang, J. Origin and elimination of photocurrent hysteresis by fullerene passivation in  $\text{CH}_3\text{NH}_3\text{PbI}_3$  planar heterojunction solar cells. *Nature Commun.* **5**, 5784 (2014).
44. Long, R., Liu, J. & Prezhdo, O. V. Unravelling the effects of grain boundary and chemical doping on electron-hole recombination in  $\text{CH}_3\text{NH}_3\text{PbI}_3$  perovskite by time-domain atomistic simulation. *J. Am. Chem. Soc.* **138**, 3884–3890 (2016).
45. Chen, Y., Peng, J., Su, D., Chen, X. & Liang, Z. Efficient and balanced charge transport revealed in planar perovskite solar cells. *ACS Appl. Mater. Interfaces* **7**, 4471–4475 (2015).
46. Li, J.-J. *et al.* Microscopic investigation of grain boundaries in organolead halide perovskite solar cells. *ACS Appl. Mater. Interfaces* **7**, 28518–28523 (2015).
47. Ishida, H., Ikeda, R. & Nakamura, D.  $^1\text{H}$  NMR studies on reorientational motions of cations in four solid phase of methylammonium iodide and the self-diffusion of ions in its highest-temperature solid phase. *Bull. Chem. Soc. Jpn* **59**, 915–924 (1986).
48. Kim, H.-S. *et al.* Control of  $I-V$  hysteresis in  $\text{CH}_3\text{NH}_3\text{PbI}_3$  perovskite solar cell. *J. Phys. Chem. Lett.* **6**, 4633–4639 (2015).
49. Jeong, W.-S., Lee, J. W., Jung, S., Yun, J. H. & Park, N.-G. Evaluation of external quantum efficiency of a 12.35% tandem solar cell comprising dye-sensitized and CIGS solar cells. *Sol. Energy Mater. Sol. Cells* **95**, 3419–3423 (2011).
50. Juška, G., Arlauskas, K., Viliūnas, M. & Kočka, J. Extraction current transients: new method of study of charge transport in microcrystalline silicon. *Phys. Rev. Lett.* **84**, 4946–4949 (2000).
51. Armin, A., Velusamy, M., Burn, P. L., Meredith, P. & Pivrikas, A. Injected charge extraction by linearly increasing voltage for bimolecular recombination studies in organic solar cells. *Appl. Phys. Lett.* **101**, 083306 (2012).
52. Dennler, G. *et al.* Charge carrier mobility and lifetime versus composition of conjugated polymer/fullerene bulk-heterojunction solar cells. *Org. Electron.* **7**, 229–234 (2006).
53. Schafferhans, J., Baumann, A., Deibel, C. & Dyakonov, V. Trap distribution and the impact of oxygen-induced traps on the charge transport in poly(3-hexylthiophene). *Appl. Phys. Lett.* **93**, 093303 (2008).
54. Juška, G., Nekrašas, N., Genevičius, K., Stuchlik, J. & Kočka, J. Relaxation of photoexcited charge carrier concentration and mobility in  $\mu\text{c-Si:H}$ . *Thin Solid Films* **451**, 290–293 (2004).

## Acknowledgements

This work was supported by the National Research Foundation of Korea (NRF) grants funded by the Ministry of Science, ICT Future Planning (MSIP) of Korea under contracts NRF-2012M3A6A7054861 and NRF-2014M3A6A7060583 (Global Frontier R&D Program on Center for Multiscale Energy System) and NRF-2012M3A7B4049986 (Nano Material Technology Development Program).

## Author contributions

N.-G.P. conceived the experiments, performed data analysis and prepared the manuscript. H.S. performed high-resolution TEM and c-AFM and wrote the relevant part. D.K. performed time-resolved PL and TA spectroscopy and wrote the relevant part. D.-Y.S. and J.-W.L. prepared materials, fabricated devices and measured photovoltaic parameters. Y.J.C. performed time-resolved PL and TA. I.-H.J. performed photo-CELIV. S.L. performed TEM and c-AFM. P.J.Y. measured AFM images. N.A. measured SEM images. M.C. commented on the SEM results and edited the manuscript. All authors discussed the results and commented on the manuscript.

## Additional information

Supplementary information is available [online](http://www.nature.com/reprints). Reprints and permissions information is available online at [www.nature.com/reprints](http://www.nature.com/reprints). Correspondence and requests for materials should be addressed to H.S., D.K. or N.-G.P.

## Competing interests

The authors declare no competing financial interests.